Bearings-Only Localization with NLOS Reflected AoAs

XIUFENG SONG
PETER WILLETT
SHENGLI ZHOU

Bearings-only localization with light-of-sight (LOS) propagation is well understood. This paper concentrates on bearings-only localization with non-line-of-sight (NLOS) measurements, where target images arrive at a network of sensors each after a single specular reflection. The reflecting surface can be 1) flat or 2) circular (inner side of a circle), and is assumed known. In this paper, we derive the least squares (LS), Stansfield, and maximum likelihood (ML) estimators for both cases. As to the former, their estimation performances are similar to their counterparts in LOS localization: Stansfield is very close to ML, and both are usually significantly better than LS. As regards the second, since the target-sensor geometry has multiple possibilities, the ML solution is extremely intricate. However, if a concentric opaque circle (such as the earth) lies within the reflecting one, e.g. the earth within the ionospheric layer, the propagation path becomes unique; a grid search based ML is available for such a circumstance. ML is computationally intensive for a circularly reflecting surface; two suboptimal algorithms, LS and Stansfield, are developed based on small angle approximation. These algorithms perform differently from those for the flat case: ML significantly outperforms LS and Stansfield, especially for a large observation error; however, Stansfield is not necessarily better than LS.

Manuscript received November 7, 2011; revised July 19, 2012; released for publication December 12, 2012.

Refereeing of this contribution was handled by Huimin Chen.

This work was supported by the U.S. Office of Naval Research under Grants N00014-07-10429 and N00014-09-10613.

Author's addresses: X. Song, LSI Corporation, 1320 Ridder Park Drive, San Jose, CA 95131, E-mail: (xiufeng.song@gmail.com); P. Willett and S. Zhou, Department of Electrical and Computer Engineering, University of Connecticut, 371 Fairfield Way U-2157, Storrs, CT 06269, E-mail: (willett@engr.uconn.edu, and shengli@engr.uconn.edu).

1557-6418/13/$17.00

1. INTRODUCTION

1.1. Distributed Localization: from LOS to NLOS

Sensor networks enable the localization of a target (or source) of interest with spatially complementary observations. Current available physical measurements include received signal strength [1], time of arrival [11], angle of arrival (AoA) [6, 7, 10, 13, 19], and so forth. They can be individually or cooperatively utilized in target information extraction. In this paper, we concentrate on localizing a single target with distributed AoAs, specifically bearings-only localization.

Bearings-only localization infers the position of a target with multiple AoA lines, which share a unique intersection—the target location—in the absence of noise. If observation uncertainty is included, a global intersection may not exist and advanced estimators are required. Least squares (LS) is a straightforward choice if the noise distribution is unknown [6]. If noise statistics are known, maximum likelihood (ML) is an option and is popular [10, 13]. Its good performance is guaranteed at the cost of computational load. The Stansfield estimator is a kind of weighted LS for independent Gaussian noise [19]; it is a compromise between estimation performance and computation. Reference [10] shows that the root mean square errors (RMSEs) of a Stansfield estimator are not necessarily larger than those of ML in bearings-only localization. Other approaches include total least squares [7], and so forth.

The aforementioned works focus on line-of-sight (LOS) propagation, where a direct path exists between the target and sensors; nevertheless, practical problems may not necessarily have a LOS. When the wavefront (acoustic, light, or electromagnetic) of target radiation meets an interface between two media, reflection will happen [14]. The reflection is helpful for the extraction of target information in some circumstances, especially where LOS propagation is unavailable. An interesting application is over-the-horizon radar (OTHR) [9, 17] (see Fig. 1). If multiple geometrically complementary radar sensors are available, a fusion center can infer the position of the target with proper data association.[1] Instead of LOS AoAs, this paper studies the localization with non-line-of-sight (NLOS) reflection measurements, where the radiation from a target reaches a sensor after a single specular reflection.

1.2. Localization with Reflected Measurements

This NLOS based localization problem is motivated by OTHR, which utilizes ionospheric reflection to capture a target beyond the horizon [9, 14, 17]. Such a reflection based technique has been used in long-range missile and aircraft detection, and it is considered an

[1] OHTRs are not the only system utilizing electromagnetic reflection phenomenon. Some other applications such as array aperture synthesis and low elevation target extraction can be respectively found in [4] and [2].

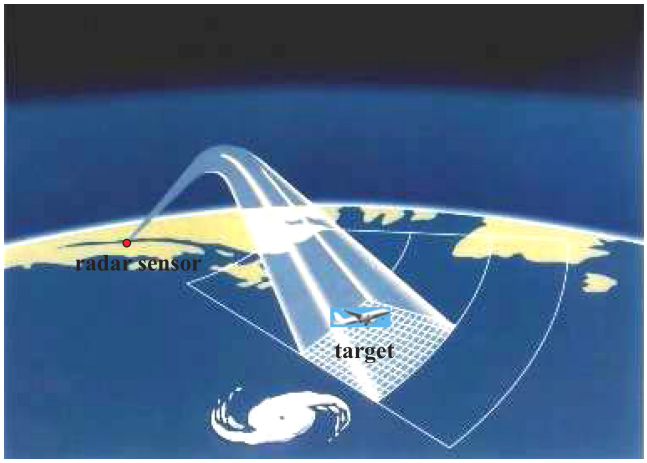

Fig. 1. An illustration of reflection based target perception with an OHTR [17].[2] The LOS path is unavailable due to the earth curvature, and the radiation of the target reaches a radar sensor after a single reflection on ionosphere. If multiple distributed radar sensors are available, one could properly associate their data to infer the location of the target.

effective means of wide-area surveillance [5]. The ionosphere has two typical reflection layers: E and F, whose characteristics are frequency dependent and resolvable [14]. In this paper, sensors are assumed to be either frequency selective or capable of resolving echo frequencies and labeling a AoA to its corresponding layer. We thus could focus on a single layer localization with multiple sensors, and the extension to double layers is straightforward. In addition, a real OTHR system works in three dimensions. This paper initiates an investigation in two dimensions—same as do [9] and [17]—where the reflection layer is the *inner* side of a circle—a slice of the ionosphere (see Fig. 3 for an immediate perception). As is the case for [9] and [17] we work in two dimensions and do not offer any discussion of incorporating the third.

As opposed to the usual LOS based localization [6, 10, 13, 19], a sensor here in the NLOS case observes the *virtual* image of a target. To understand the ramifications thoroughly, we investigate in two steps: *flat* and *circular* reflecting surfaces, where the reflection is assumed to be specular [9]. The ML, Stansfield, and LS algorithms are derived for both cases. Even though the former does not have a clear physical application, it facilitates the importation, from conventional LOS based localization [6, 10, 13, 19] ideas, to the latter situation of NLOS based localization with circular reflected AoAs.

As for a flat surface, the target-sensor reflection geometry is unique, and we show that:

- the algorithm comparison for the LOS case in [6], [10], [13], [19] still holds here: LS has the worst performance, while the RMSE of Stansfield estimator is not necessarily larger than that of ML.

[2]Reference [17] acknowledges that the picture is in turn derived from an image provided by the US National Oceanic and Atmospheric Administration (NOAA).

TABLE I
Coordinates Notions

Coordinate	Objective
(x_t, y_t)	target
(x_i^s, y_i^s)	the ith sensor
$(\bar{x}_i^t, \bar{y}_i^t)$	image of (x_t, y_t) corresponding to the ith mirror
$(\bar{x}_i^s, \bar{y}_i^s)$	image of (x_i^s, y_i^s) corresponding to the ith mirror
$(\bar{x}_i^n, \bar{y}_i^n)$	image of (x_i^s, y_i^s) corresponding to the normal line
(x_i^c, y_i^c)	intersection between circle and the ith observation line
(x_b, y_b)	boundary of blocking circle division area

The circular NLOS case has two unique properties: 1) the reflection with a circular surface is nonlinear, and the image of a single point with respect to it is not unique; 2) the spatial uncertainty of the target does not coincide with that of the AoA, since the circular reflection nonlinearly changes the noise spatial distribution around the target (a focusing effect, see Fig. 7). That is, circular/NLOS is considerably more complicated than flat/LOS, and this paper investigates it from the following perspectives:

- We give the reflection model and reveal that multiple reflection paths exist between a sensor and the target. A ML solution turns out to be quite intricate.
- If an opaque blocking circle (no propagation can pass through it) is concentric to the reflecting one, and all the sensors are deployed on the blocking circle, then the unblocked target-sensor reflection path is unique and can be found numerically. Therefore, a grid search based ML can be performed.
- The grid search is laborious; suboptimal algorithms such as LS and Stansfield are given based on a small arc approximation. Their performance are compared.

Note that the suboptimal algorithms for the circular reflection case utilize the corresponding results of the flat case.

This paper includes some material from [18], however, with significant expansions including a thorough investigation of flat reflecting surface and explicit target-sensor geometric analysis for circular reflecting surface. The rest of this paper is as follows. Section 2 studies the bearings-only localization with flat reflecting surfaces; Section 3 analyzes the reflection geometry for a circular surface, and gives the ML localization algorithm; suboptimal localization approaches for circular reflection are given in Section 4; numerical results are in Section 5, while conclusions are drawn after that.

Notation: Boldface uppercase and lowercase letters denote matrices and column vectors respectively. $\|\cdot\|$ stands for the Frobenius norm, while diag($\mathbf{a}$) denotes the diagonal matrix formed by vector $\mathbf{a}$. $(\cdot)^T$ and $(\cdot)^{-1}$, respectively, represent matrix transpose and inverse. $\overline{AB}$ and $\widehat{AB}$ respectively denote the line and arc through points A and B, while $\angle\widehat{AB}$ measures the angle of $\widehat{AB}$. $\mathcal{N}(0, \varepsilon^2)$ is a zero-mean Gaussian distribution with variance ε^2. Finally, the coordinates of different locations are collected in Table I for clarity.

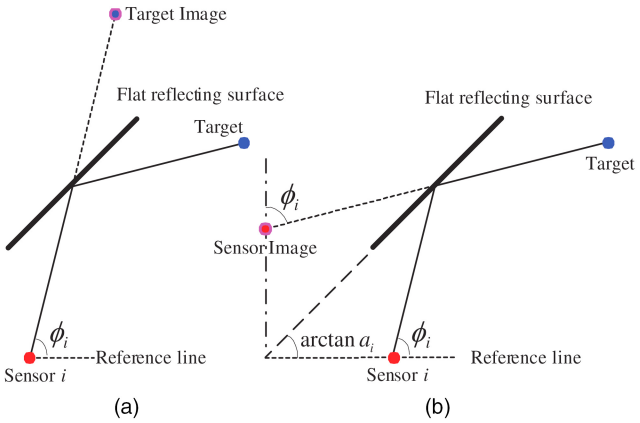

Fig. 2. Bearings-only measurement with flat reflecting surface: (a) target image based modeling, and (b) sensor image based modeling.

2. BEARINGS-ONLY LOCALIZATION WITH FLAT REFLECTING SURFACES

This section investigates NLOS localization with known *flat* reflection surfaces, where a LOS propagation path is assumed unavailable. The radiations of a target arrive at a network of passive sensors after a single specular reflection, and the AoA is recorded by an individual sensor. Suppose that proper synchronization and communication links are extant, and hence a processing center can collect the reflected AoAs to infer the location of target.

2.1. Maximum Likelihood Estimation

ML with flat reflecting surfaces has two modeling approaches: target and sensor images based (see Fig. 2). In the following, we will show their equivalence.

2.1.1. Target Image Based Modeling

If a reflecting surface is flat, the image of a target is unique. A sensor actually observes the target image instead of the target itself. Therefore, the image based modeling as shown in Fig. 2(a) is obvious.

Let the coordinates of the target be (x_t, y_t), and then the location of its image with respect to a reflecting surface $y = a_i x + b_i$ is expressed as $(\bar{x}_i^t, \bar{y}_i^t)$, where

$$\begin{aligned} \bar{x}_i^t &= \frac{1-a_i^2}{1+a_i^2}x_t + \frac{2a_i}{1+a_i^2}y_t - \frac{2a_i b_i}{1+a_i^2} \\ \bar{y}_i^t &= \frac{2a_i}{1+a_i^2}x_t + \frac{a_i^2-1}{1+a_i^2}y_t + \frac{2b_i}{1+a_i^2} \end{aligned} \tag{1}$$

based on Lemma 4 in Appendix A. As a result, the measured AoA for the ith sensor is

$$\varphi_i = \underbrace{\arctan\left(\frac{\bar{y}_i^t - y_i^s}{\bar{x}_i^t - x_i^s}\right)}_{\triangleq \phi_i'(x_t, y_t)} + n_i' \tag{2}$$

where (x_i^s, y_i^s) stands for the (known) coordinates of sensor i, and n_i' denotes its measurement noise.

2.1.2. Sensor Image Based Modeling

The measured AoA can be transformed as a function of sensor image as shown in Fig. 2(b). Let the reflecting surface be $y = a_i x + b_i$, and then the slope of the image of horizontal reference line is $\tan(2a_i)$. Therefore, the observed AoA for sensor i is written as

$$\varphi_i = \underbrace{2\arctan a_i - \arctan\left(\frac{y_t - \bar{y}_i^s}{x_t - \bar{x}_i^s}\right)}_{\triangleq \phi_i(x_t, y_t)} + n_i \tag{3}$$

where $(\bar{x}_i^s, \bar{y}_i^s)$ denotes the coordinates of the image of sensor i corresponding to $y = a_i x + b_i$,

$$\begin{aligned} \bar{x}_i^s &= \frac{1-a_i^2}{1+a_i^2}x_i^s + \frac{2a_i}{1+a_i^2}y_i^s - \frac{2a_i b_i}{1+a_i^2} \\ \bar{y}_i^s &= \frac{2a_i}{1+a_i^2}x_i^s + \frac{a_i^2-1}{1+a_i^2}y_i^s + \frac{2b_i}{1+a_i^2} \end{aligned} \tag{4}$$

and n_i represents the noise for sensor image based modeling. Note that the $(\bar{x}_i^s, \bar{y}_i^s)$s can be precalculated.

The measurement uncertainty of the second approach n_i is an imaging transformation of that for the first one n_i'. If the reflecting surface is flat, the transformation will not change the distribution. Based on Appendix B, we obtain $\phi_i(x_t, y_t) = \phi_i'(x_t, y_t)$, so the two modeling approaches are equivalent. As for the first one, the unknown parameters, x_t and y_t, are included in both the numerator and denominator of $\tan\phi_i'(x_t, y_t)$; direct optimization with it will have a nontrivial computational load. The following estimation algorithms adopt the second modeling approach.

Suppose that the measurement uncertainty of sensor i subjects to zero-mean Gaussian distribution with variance σ_i^2. Collecting the unknown parameters as $\boldsymbol{\theta} = [x_t, y_t]^T$, the conditional probability density function (PDF) of the observed AoA for the ith sensor is

$$f(\varphi_i \mid \boldsymbol{\theta}) = \frac{1}{\sqrt{2\pi\sigma_i^2}} \exp\left(-\frac{|\varphi_i - \phi_i|^2}{2\sigma_i^2}\right) \tag{5}$$

where $\phi_i \triangleq \phi_i(x_t, y_t)$ for notational simplicity. Let each sensor send its bearing measurement to a central processing unit, and then the central processor utilizes all of them to estimate target location. Suppose that $f(\varphi_i \mid \boldsymbol{\theta})$s are mutually independent; the centralized ML estimator is given by

$$\begin{aligned} \hat{\boldsymbol{\theta}}_{\mathrm{ML}} &= \arg\max_{\boldsymbol{\theta}} \prod_{i=1}^{N} f(\varphi_i \mid \boldsymbol{\theta}) \\ &= \arg\min_{\boldsymbol{\theta}} \sum_{i=1}^{N} \frac{1}{\sigma_i^2} |\varphi_i - \phi_i|^2 \end{aligned} \tag{6}$$

where N counts the number of sensors.

2.2. Stansfield Estimation

Stansfield estimator approximates ML under small observation errors [19]. It relies on *the law of small-*

angle approximation: the bearing noise n_i is small enough that

$$n_i \approx \sin n_i. \tag{7}$$

Substituting (3) into (7), we have

$$\varphi_i - \phi_i \approx \sin(\varphi_i - \phi_i) \tag{8}$$

$$= \sin\left(\underbrace{\varphi_i - 2\arctan a_i}_{\triangleq \gamma_i} + \arctan\left(\frac{y_t - \bar{y}_i^s}{x_t - \bar{x}_i^s}\right)\right)$$

$$= \frac{(x_t - \bar{x}_i^s)\sin\gamma_i + (y_t - \bar{y}_i^s)\cos\gamma_i}{d_i(x_t, y_t)}. \tag{9}$$

Substituting (9) into (6), the optimization is recast as

$$\hat{\boldsymbol{\theta}}_{\mathrm{SE}} = \arg\min_{\boldsymbol{\theta}} (\mathbf{U}\boldsymbol{\theta} - \mathbf{v})^T \boldsymbol{\Lambda}^{-1} \mathbf{D}^{-1} (\mathbf{U}\boldsymbol{\theta} - \mathbf{v}) \tag{10}$$

where $\boldsymbol{\Lambda} = \mathrm{diag}([\sigma_1^2, \ldots, \sigma_N^2])$,

$$\mathbf{U} = \begin{bmatrix} \sin\gamma_i & \cos\gamma_i \\ \vdots & \vdots \\ \sin\gamma_N & \cos\gamma_N \end{bmatrix} \tag{11}$$

is a $N \times 2$ matrix assumed with full rank,

$$\mathbf{v} = \begin{bmatrix} \bar{x}_1^s \sin\gamma_1 + \bar{y}_1^s \cos\gamma_1 \\ \vdots \\ \bar{x}_N^s \sin\gamma_N + \bar{y}_N^s \cos\gamma_N \end{bmatrix} \tag{12}$$

and

$$\mathbf{D} = \mathrm{diag}([d_1^2(x_t, y_t), \ldots, d_N^2(x_t, y_t)]) \tag{13}$$

where $d_i(x_t, y_t)$ denotes the distance between the target and the image of the ith sensor:

$$d_i(x_t, y_t) \triangleq \sqrt{(x_t - \bar{x}_i^s)^2 + (y_t - \bar{y}_i^s)^2}. \tag{14}$$

Clearly, the distance matrix $\mathbf{D}$ depends on target location (x_t, y_t), and it is unknown.

In [19], the distance matrix $\mathbf{D}$ is assumed available from secondary observations; therefore, (10) degenerates to a standard quadratic optimization. Later, [10] shows that a rough estimate, say $\hat{\mathbf{D}}$, can be used in (10) without significantly affecting the estimation accuracy, because its objective function only weakly relies on $\mathbf{D}$. With $\hat{\mathbf{D}}$, the solution for (10) is

$$\hat{\boldsymbol{\theta}}_{\mathrm{SE}} = (\mathbf{U}^T \boldsymbol{\Lambda}^{-1} \hat{\mathbf{D}}^{-1} \mathbf{U})^{-1} \mathbf{U}^T \boldsymbol{\Lambda}^{-1} \hat{\mathbf{D}}^{-1} \mathbf{v} \tag{15}$$

which has the form of weighted LS.

2.3. Least Squares Initialization

Both ML and Stansfield estimators require a guess of $\boldsymbol{\theta}$: the former uses it for optimization initialization, while the latter employs it to obtain $\hat{\mathbf{D}}$. This can be realized via LS.

The line through the target and the image of sensor i is

$$y - \bar{y}_i^s = \tan(\underbrace{2\arctan a_i - \varphi_i}_{=-\gamma_i})(x - \bar{x}_i^s) \tag{16}$$

equivalently written as

$$(x - \bar{x}_i^s)\sin\gamma_i + (y - \bar{y}_i^s)\cos\gamma_i = 0. \tag{17}$$

Therefore, one can minimize

$$\hat{\boldsymbol{\theta}}_{\mathrm{LS}} = \arg\min_{x,y} \left\{ \sum_{i=1}^{N} |(x - \bar{x}_i^s)\sin\gamma_i + (y - \bar{y}_i^s)\cos\gamma_i|^2 \right\}$$

$$= \arg\min_{\boldsymbol{\theta}} \|\mathbf{U}\boldsymbol{\theta} - \mathbf{v}\|^2 \tag{18}$$

$$= (\mathbf{U}^T\mathbf{U})^{-1}\mathbf{U}^T\mathbf{v} \tag{19}$$

to get an initial guess of $\boldsymbol{\theta}$. Here $\mathbf{U}$ and $\mathbf{v}$ share the same definitions as those in the previous subsection.

2.4. Cramér-Rao Lower Bound

The Cramér-Rao lower bound (CRLB) reveals performance limitation of an unbiased estimator. For a non-random vector $\boldsymbol{\theta}$, its estimation covariance matrix is bounded by [15]

$$\mathbb{E}\{(\hat{\boldsymbol{\theta}} - \boldsymbol{\theta})(\hat{\boldsymbol{\theta}} - \boldsymbol{\theta})^T\} \geq \mathbf{J}_{\boldsymbol{\theta}}^{-1} \tag{20}$$

where $\mathbf{J}_{\boldsymbol{\theta}}$ is the Fisher information matrix defined as

$$\mathbf{J}_{\boldsymbol{\theta}} = -\mathbb{E}\left\{ \nabla_{\boldsymbol{\theta}} \left[\nabla_{\boldsymbol{\theta}} \log\left(\prod_{i=1}^{N} f(\varphi_i \mid \boldsymbol{\theta}) \right) \right]^T \right\}$$

$$= \sum_{i=1}^{N} \frac{1}{2\sigma_i^2} \mathbb{E}\{\nabla_{\boldsymbol{\theta}} (\nabla_{\boldsymbol{\theta}} \underbrace{|\varphi_i - \phi_i|^2}_{\triangleq P_i})^T\}. \tag{21}$$

Clearly, $\mathbf{J}_{\boldsymbol{\theta}}$ is a 2×2 matrix, and we now specify it element-by-element. The first-order derivatives of P_i are

$$\frac{\partial P_i}{\partial x_t} = 2(\phi_i - \varphi_i)\frac{\partial \phi_i}{\partial x_t} \quad \text{and} \quad \frac{\partial P_i}{\partial y_t} = 2(\phi_i - \varphi_i)\frac{\partial \phi_i}{\partial y_t}. \tag{22}$$

Recall the definition of $d_i(x_t, y_t)$ in (14), and then $\partial\phi_i/\partial x_t$ and $\partial\phi_i/\partial y_t$ shall be specified as

$$\frac{\partial \phi_i}{\partial x_t} = \frac{y_t - \bar{y}_i^s}{d_i^2(x_t, y_t)} \quad \text{and} \quad \frac{\partial \phi_i}{\partial y_t} = -\frac{x_t - \bar{x}_i^s}{d_i^2(x_t, y_t)}. \tag{23}$$

Based on (22), the second order derivatives of P_i are

$$\frac{\partial^2 P_i}{\partial^2 x_t} = 2\left(\frac{\partial \phi_i}{\partial x_t}\right)^2 + 2(\phi_i - \varphi_i)\frac{\partial^2 \phi_i}{\partial^2 x_t} \tag{24}$$

$$\frac{\partial^2 P_i}{\partial^2 y_t} = 2\left(\frac{\partial \phi_i}{\partial y_t}\right)^2 + 2(\phi_i - \varphi_i)\frac{\partial^2 \phi_i}{\partial^2 y_t} \tag{25}$$

$$\frac{\partial^2 P_i}{\partial x_t \partial y_t} = \frac{\partial^2 P_i}{\partial y_t \partial x_t} = 2\frac{\partial \phi_i}{\partial x_t}\frac{\partial \phi_i}{\partial y_t} + 2(\phi_i - \varphi_i)\frac{\partial^2 \phi_i}{\partial x_t \partial y_t}. \tag{26}$$

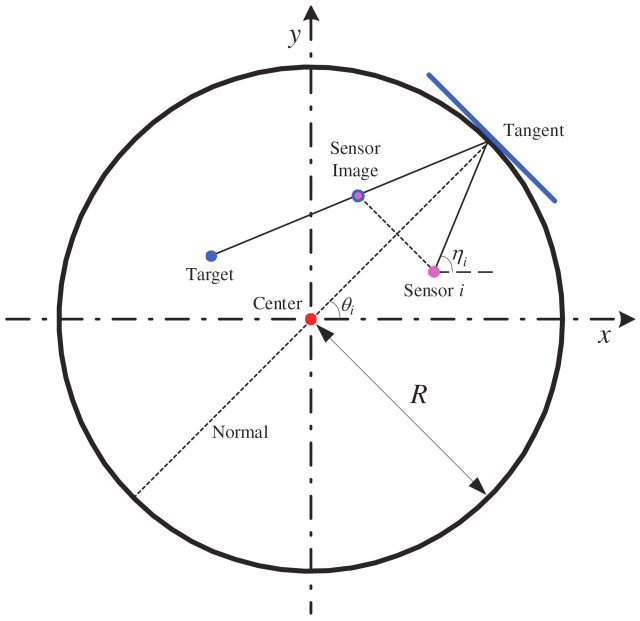

Fig. 3. AoA measurement with circular reflecting surface: the radiation of the target arrives at a sensor after a single specular reflection. The reflection geometry can be equivalently addressed as that the image of sensor with respect to the reflecting normal is exactly on the line determined by target and reflection point.

Since $\mathbb{E}\{\phi_i - \varphi_i\} = 0$, we obtain

$$[\mathbf{J}_{\boldsymbol{\theta}}]_{1,1} = \sum_{i=1}^{N} \frac{1}{\sigma_i^2} \left(\frac{\partial \phi_i}{\partial x_t} \right)^2 \tag{27}$$

$$[\mathbf{J}_{\boldsymbol{\theta}}]_{2,2} = \sum_{i=1}^{N} \frac{1}{\sigma_i^2} \left(\frac{\partial \phi_i}{\partial y_t} \right)^2 \tag{28}$$

$$[\mathbf{J}_{\boldsymbol{\theta}}]_{1,2} = [\mathbf{J}_{\boldsymbol{\theta}}]_{2,1} = \sum_{i=1}^{N} \frac{1}{\sigma_i^2} \left(\frac{\partial \phi_i}{\partial x_t} \cdot \frac{\partial \phi_i}{\partial y_t} \right) \tag{29}$$

where $[\mathbf{J}_{\boldsymbol{\theta}}]_{j,k}$ refers to a particular element of $\mathbf{J}_{\boldsymbol{\theta}}$.

3. BEARINGS-ONLY LOCALIZATION WITH CIRCULAR REFLECTING SURFACE

The reflecting surface was flat in the previous section. Now we will focus on bearings-only localization with a circular reflecting surface (inner side of a circle), where the target and N sensors are all within a circle as depicted in Fig. 3. The radiation from the target reaches each sensor after a single specular reflection on the circle, where the reflection is assumed to be specular [9]. A fusion center collects the noisy AoAs to infer the target position. Note that some similar problems exist in elastic collision and optical imaging [8, 12, 16]; results of this paper may be useful in their cases, especially where there is noise.

3.1. Geometric Modeling

The geometric relationships between the target and sensors are required for localization. Suppose the reflection be specular, so the angle of incidence equals the angle of reflection. Let the center of the reflecting circle be $(x_c = 0,\ y_c = 0)$, and let $(R\cos\theta_i, R\sin\theta_i)$ stand for the (unknown) reflection point for sensor i, where R denotes the radius of the circle, and θ_i is an instrumental variable as shown in Fig. 3. Instead of direct application of the reflection law, we use an equivalent transformation: the image of sensor i corresponding to the normal line

$$y = x\tan\theta_i \tag{30}$$

is exactly on the line through target and reflection point as shown in Fig. 3. Mathematically, it is expressed as

$$\frac{R\cos\theta_i - \bar{x}_i^n}{R\sin\theta_i - \bar{y}_i^n} = \frac{x_t - R\cos\theta_i}{y_t - R\sin\theta_i} \tag{31}$$

where (x_t, y_t) denotes the coordinates of the target, while $(\bar{x}_i^n, \bar{y}_i^n)$ denotes the image coordinates of the ith sensor with respect to the normal line. As the coordinates of the ith sensor is (x_i^s, y_i^s), and hence $(\bar{x}_i^n, \bar{y}_i^n)$ can be written as

$$\begin{aligned} \bar{x}_i^n &= \cos(2\theta_i)x_i^s + \sin(2\theta_i)y_i^s \\ \bar{y}_i^n &= \sin(2\theta_i)x_i^s - \cos(2\theta_i)y_i^s \end{aligned} \tag{32}$$

based on Appendix A. Substituting (32) into (31), we have

$$\frac{R(y_i^s + y_t)\cos\theta_i - R(x_i^s + x_t)\sin\theta_i}{(x_i^s y_t + x_t y_i^s)\cos(2\theta_i) - (x_i^s x_t - y_i^s y_t)\sin(2\theta_i)} = 1. \tag{33}$$

Now, the coordinate connection between sensor i and target is obtained with the help of θ_i.

3.2. Maximum Likelihood Estimation

Suppose that θ_i could be expressed as a function of x_t and y_t, say $\theta_i(x_t, y_t)$, and then we can choose the reflection point $(R\cos(\theta_i(x_t, y_t)), R\sin(\theta_i(x_t, y_t)))$ as a reference and formulate the observed AoA ψ_i as

$$\psi_i = \underbrace{\arctan\left(\frac{R\sin(\theta_i(x_t, y_t)) - y_i}{R\cos(\theta_i(x_t, y_t)) - x_i} \right)}_{\triangleq \eta_i(x_t, y_t)} + w_i \tag{34}$$

where $w_i \sim \mathcal{N}(0, \varepsilon_i^2)$ denotes the Gaussian measurement noise. Let the w_is be independent, and hence the ML estimation becomes

$$\hat{\boldsymbol{\theta}} = \arg\max_{\boldsymbol{\theta}} \prod_{i=1}^{N} f(\psi_i \mid \boldsymbol{\theta}), \tag{35}$$

where

$$f(\psi_i \mid \boldsymbol{\theta}) = \frac{1}{\sqrt{2\pi\varepsilon_i^2}} \exp\left(-\frac{|\psi_i - \eta_i(x_t, y_t)|^2}{2\varepsilon_i^2} \right) \tag{36}$$

denotes the conditional probability density function of ψ_i.

3.3. Challenges for Maximum Likelihood

To this point all appears as the (straightforward?) LOS localization case. What is new? Three things are:

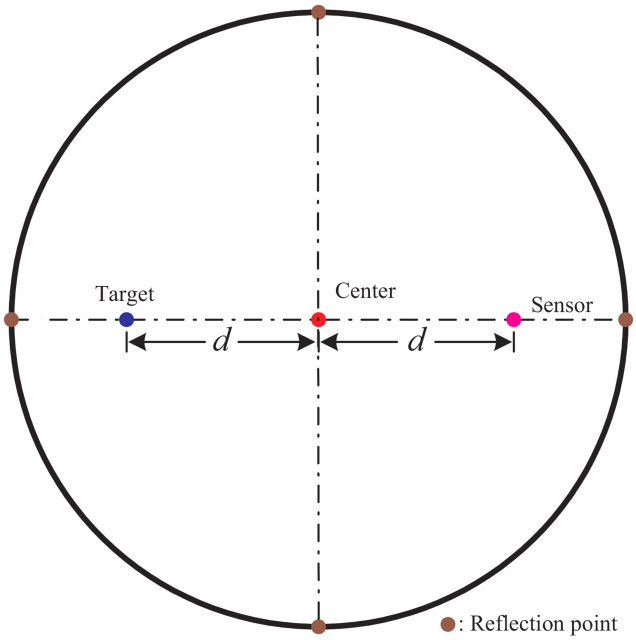

Fig. 4. An illustration of the existence of multiple solutions for (33). If a target and a sensor is symmetric about the center of the reflection circle, four reflection points can be immediately found. Note that reflection points are not necessarily as uniform as those in the figure if the sensor and the target is not centrally symmetric.

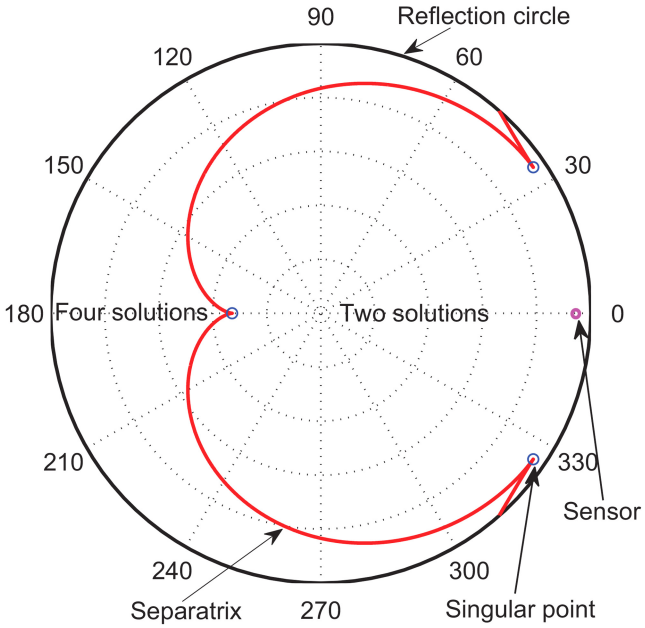

Fig. 5. Solution number distribution within a unit circle: a sensor is fixed at ($x_i^s = 0.955$, $y_i^s = 0$), while a target can be arbitrarily selected within it. If the target is located in the *two (four) solutions* region, equation (33) has two (four) possible nonoverlapping reflection paths, while if the target is on the separatrix line, equation (33) has three solutions. The sensor and the right two singular points are concentric.

1) The solution $\theta_i(x_t, y_t)$ is not unique. Therefore, the expression of (34) is not unique, neither is the likelihood equation (35). An example with a special target-sensor configuration is provided in Fig. 4 for illustration.

2) The number of $\theta_i(x_t, y_t)$ depends on geometry—the locations of target and sensor i.

3) $\theta_i(x_t, y_t)$ cannot be analytically obtained; thus, a closed-form expression of likelihood equation is unavailable.

A thorough understanding of these is important to understand the ML formulation in (35). The first two points relate to a famous geometric problem—circular billiards. Reference [8] gives a comprehensive analysis on the solution properties of (33) for a normalized circle, and we briefly summarize them below for completeness.

LEMMA 1 *Let* ($x_c = 0$, $y_c = 0$) *and* $R = 1$. *A sensor is fixed at* ($x_i^s = c$, $y_i^s = 0$), *where* $0 \le c < 1$, *while the target* (x_t, y_t) *is arbitrarily located within the circle. If* $|c| + |x_t| + |y_t| \neq 0$, *the number of solutions for* (33) *is either 2, 3, or 4 for a given* (x_t, y_t). *Furthermore, define a supplementary variable* h *as*

$$h = (1 - 3c + 2c^2)t^6 + 3(1 - c + 2c^2)t^4 + 3(1 + c + 2c^2)t^2 + (1 + 3c + 2c^2) \quad (37)$$

where $t \in [-\infty, +\infty]$, *and then the separatrix* $l(x, y)$

$$x = -\frac{c}{h}[(1 - c)t^6 + 3(1 - 3c)t^4 + 3(1 + 3c)t^2 + (1 + c)]$$
$$y = \frac{16c^2t^3}{h} \quad (38)$$

divides the circle into two parts. If the target falls into the region that includes point $(0,0)$, (33) *has two solutions, while if it falls into the other one, the number of solutions for* (33) *is four. Finally, if the target falls (exactly) on* $l(x, y)$, (33) *has three solutions.*

PROOF Proof can be found in [8].

Clearly, the shape of $l(x, y)$ depends on the value of c. An illustration with $c = 0.955$ is given in Fig. 5. From this figure, we see that $l(x, y)$ is continuous but not everywhere differentiable; a nondifferentiable point is denoted singularity [8]. For $|c| \ge 1/3$, $l(x, y)$s share the similar shape as that in Fig. 5: the separatrix is open and has three singular points: ($x = -c/(1 + 2c)$, $y = 0$) and

$$\left(x = c(2c^2 - 1),\ y = \pm 2c^2\sqrt{1 - c^2}\right). \quad (39)$$

Those for $|c| < 1/3$ share another shape, where the separatrix is closed, and another singular point ($x = -c/(1 - 2c)$, $y = 0$) is added in addition to the previous three. Note that 1) the above results are valid for $R = 1$ and $y_i^s = 0$; any other scenario with $R \neq 1$ or (and) $y_i^s \neq 0$ can be obtained via a simple scaling or (and) rotation of coordinates; 2) Lemma 1 does not include the extreme case, $c = x_t = y_t = 0$, of which the number of solutions is infinity.

The first two points are now clear. The geometrically dependent multiple-solution characteristics of circular reflection can significantly complicate ML estimation. For example, if a sensor obtains a noisy AoA, it may be

responsible for up to 4 propagation paths. Since we have no knowledge to which one the AoA corresponds, a complete case-by-case enumeration is necessary in ML processing. As a result, for a system with N sensors, the total number of possible combinations can be up to 4^N. The final ML result is the best estimate from all these combinations; obviously, it is very intricate.

Regarding the third item, $\theta_i(x_t, y_t)$ cannot be analytically derived, nor can the likelihood maximization (35) be explicitly posed. As a consequence, local search algorithms such as gradient-based approaches [3] and alternating projection [21] will not in general work here. Fortunately, since the $\theta_i(x_t, y_t)$s can be numerically calculated for a given (x_t, y_t), a grid search based algorithm [20] is applicable for this problem. Specifically, uniformly divide a search area around the initial guess into a fine grid, and pick up the grid cell with the maximum ML value as an optimal estimate. This algorithm works well for low dimensions, and its performance depends on grid fineness, the search area size, and the accuracy of initialization. Generally, the larger the search area and the greater the fineness, the better performance; however, the larger the search area, the greater the computational load.

3.4. Maximum Likelihood Simplification with a Blocking Circle

In the previous subsection, target and sensors are arbitrarily located within the enclosing reflection circle; nevertheless, a real problem has more physical constraints. For example, the earth serves as a blocking (opaque) circle; no radiation can pass through it. Furthermore, the sensors are likely fixed on the earth, while the target is always within the annulus between the two circles. Suppose the reflection and blocking circles be concentric; we will show that the ML estimation could be simplified with the above constraints.

LEMMA 2 *Let the radius of the blocking circle be r, where $r < R$. Suppose a sensor be at A as shown in Fig. 6. Let $\overline{AC}$ and $\overline{CD}$ be two tangents of the blocking circle, and then we have that:*

- *if the target is located within region $\mathcal{A}_1$, enclosed by $\overline{CD}$, $\widehat{DE}$, $\overline{EF}$, and $\widehat{CF}$, it is reflectively-invisible for the sensor; or*
- *if the target is located within region $\mathcal{A}_2$, enclosed by $\overline{AB}$, $\widehat{BC}$, $\overline{CD}$, and $\widehat{AD}$, it is reflectively-visible for the sensor.*

PROOF Let T be an arbitrary point within $\mathcal{A}_1$, and assume $\overline{AG}$–$\overline{GT}$ be an unblocked reflection path, where G denotes the reflection point. To guarantee $\overline{AG}$ be free from blocking, G must be located on arc $\widehat{BC}$. Due to the symmetry of specular reflection, $\overline{GT}$ will have an intersection, say H, with the blocking circle. Therefore, we have $\angle\widehat{AH} = 2\angle\widehat{BG} < 2\angle\widehat{BC} = \angle\widehat{AD}$, and H is located on arc $\widehat{AD}$. As a result, line $\overline{GH}$, or, $\overline{GT}$ could not go through $\mathcal{A}_1$. Obviously, this contradicts the assumption, so an unblocked reflection path does not exist for the first case.

The proof of the second conclusion is trivial. If a reflection point, say J, continuously moves from C to B on arc $\widehat{BC}$, the intersection between the reflection line and inner circle, say K, will continuously go from D to A. Line $\overline{JK}$ will go through the entire $\mathcal{A}_2$. Therefore, every point within $\mathcal{A}_2$ is visible, and Lemma 2 holds.

A half-plane is employed in Lemma 2, and the other part is the same due to symmetry. The reflectively-visible area $\mathcal{A}_2$ includes a LOS-visible region $\mathcal{A}_3$, which is enclosed by $\overline{AB}$, $\widehat{BC}$, and $\overline{AC}$. If a target falls into $\mathcal{A}_3$ of each sensor,[3] direct arrivals will be utilized to estimate the position of the target, and hence the problem becomes a conventional LOS bearings-only localization [6, 10, 13, 19]. A mixed scenario, parts of sensors obtaining LOS while the others measuring NLOS reflective AoAs, is also physically sound. Its localization can be easily realized via a proper modification of (35), and no discussion or specific example will be given. In addition, since a real system requires a certain amount of elevation angle to avoid ground clutter, the practical reflectively- and LOS-visible areas are smaller than their theoretical results $\mathcal{A}_2$ and $\mathcal{A}_3$.

LEMMA 3 *If the sensor is deployed at $(r, 0)$ while the target is arbitrarily located within the reflectively-visible region $\mathcal{A}_1$, then the sensor-target pair has exactly one unblocked reflective path.*

PROOF Firstly, we will show that the reflectively-visible region $\mathcal{A}_1$ and the *four-solution region* shares no subarea with the help of Fig. 5 and 6. Since $\angle\widehat{AD} = \angle\widehat{BC} = 2\arccos r/R$, the coordinates of boundary point D, say (x_d, y_d), is

$$\begin{aligned} x_d &= r\cos\angle\widehat{AD} = r\left(2\frac{r^2}{R^2} - 1\right) \\ y_d &= r\sin\angle\widehat{AD} = 2\frac{r^2}{R^2}\sqrt{R^2 - r^2}. \end{aligned} \tag{40}$$

Normalize (x_d, y_d) with R, say (x'_d, y'_d), and define $c = r/R$; we see that (x'_d, y'_d) is exactly the upper singular point of the separatrix as shown in (39). For a half-plane as depicted in Fig. 6, since the four-solution region is always on the left side of line $\overline{OD}$ [8], and since the reflectively-visible region $\mathcal{A}_1$ is on its right side, their intersection is empty. In the other words, $\mathcal{A}_1$ falls into the *two-solution region* as shown in Fig. 5. Moreover, the

[3]The ionosphere is frequency selective, and only a certain frequency span is useful for beyond-horizon exploration. For a real configuration, an OTHR site is in general accompanied with another radar system equipped with a non-ionospheric-reflection frequency. Their detection results are combined to infer the target status: 1) if both of them claim a target in a certain direction, the target actually appears in $\mathcal{A}_3$; however, 2) if only the OTHR declares a detection, the target is beyond the horizon. One can properly use such information to mitigate area uncertainty before target localization.

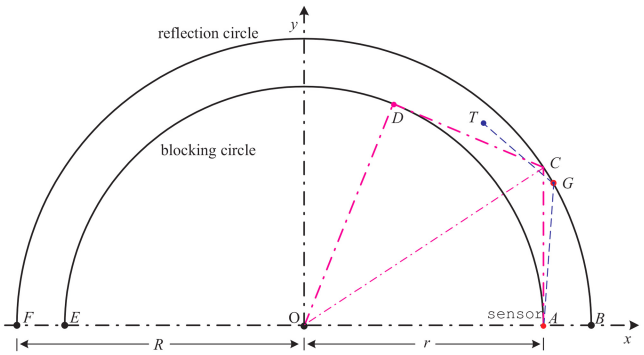

Fig. 6. Reflectively-visible and -invisible areas within in the annulus between the reflection and blocking circles. The sensor is located at $(r,0)$, while the target can be arbitrarily within the annulus. If the target falls into $\mathcal{A}_1$, the area bounded by $\overline{CD}$, $\widehat{DE}$, $\overline{EF}$, and $\widehat{CF}$, its radiation cannot arrive at sensor after one reflection. However, if it falls into $\mathcal{A}_2$, the area enclosed by $\overline{AB}$, $\widehat{BC}$, $\overline{CD}$, and $\widehat{AD}$, the target is reflectively-visible. Note that $\overline{AC}$ and $\overline{CD}$ are two tangents of the blocking circle, while $\overline{AG}$ and $\overline{GT}$ are two supplementary lines in the proof of area division.

two reflection paths are separated by the line through the sensor and target [8]; therefore, one of them will be blocked. As a result, Lemma 3 can be proven.

With a blocking circle, only one solution of (33) is valid; the likelihood equation (35) is unique for a given grid sample. As a consequence, the grid search based ML can be significantly simplified. Note that since a closed-form likelihood function is unavailable, the CRLB will not be given for the circular reflecting surface.

4. SUBOPTIMAL ESTIMATION FOR CIRCULAR REFLECTING SURFACE

Grid search based ML may obtain a globally optimal estimate of a target; however, its computational complexity is extremely high, as N calculations of $\theta_i(x_t,y_t)$ are required for even one grid point. Suboptimal algorithms with low computational load are investigated in this section based on a *small-angle approximation*. The basic idea is simple: if a sensor is close to the surface of a circle with large radius, and its observation variance is small, then the arc corresponding to the measurement uncertainty has a small angle. Approximate it as flat, and the tangent line through the intersection between the ith AoA and the reflection circle can be considered as a known flat reflecting surface.

Let the observed AoA of the ith sensor be ψ_i; its corresponding observation line, say l_i^o, can be expressed as

$$y = (x - x_i^s)\tan\psi_i + y_i^s. \tag{41}$$

The observation line l_i^o intersects the reflecting circle $x^2 + y^2 = R^2$ at two points (x_i^c, y_i^c), where

$$\begin{aligned} x_i^c &= \cos^2\psi_i[\tan\psi_i(x_i^s\tan\psi_i - y_i^s) \pm K_i] \\ y_i^c &= \cos^2\psi_i[(y_i^s - x_i^s\tan\psi_i) \pm K_i\tan\psi_i] \end{aligned} \tag{42}$$

and

$$K_i = \sqrt{R^2/\cos^2\psi_i - (y_i^s - x_i^s\tan\psi_i)^2}. \tag{43}$$

Since the observation line is a ray, one solution of (42) can easily be removed. The tangent line through the intersection (x_i^c, y_i^c), say l_i^t, is

$$y = -\frac{x_i^c}{y_i^c}(x - x_i^c) + y_i^c \tag{44}$$

and it can be regarded as a 'known' flat reflecting surface to localize a target with LS or Stansfield algorithms in Section 2 via proper slope and intercept mappings:

$$\begin{aligned} a_i &= -x_i^c/y_i^c \\ b_i &= (x_i^c)^2/y_i^c + y_i^c. \end{aligned} \tag{45}$$

Based on these, the suboptimal LS and Stansfield localization algorithms are briefly summarized below:

1) Get the AoA lines l_i^o for each sensor with (41);
2) Calculate the intersections (x_i^c, y_i^c)s between l_i^os and the reflection circle with (42);
3) Compute a_i and b_i for each tangent line l_i^t with (45);
4) Take l_i^t as a flat reflecting surface, and compute the image coordinate, say $(\bar{x}_i^s, \bar{y}_i^s)$, of sensor i with (4);
5) Substitute a_is, b_is and $(\bar{x}_i^s, \bar{y}_i^s)$s into (11) and (12) and compute $\mathbf{U}$ and $\mathbf{v}$;
6a) LS: Consider $(\bar{x}_i^s, \bar{y}_i^s)$s as a virtual sensor, and estimate $\hat{\boldsymbol{\theta}}_{\mathrm{LS}}$ with (19).
6b) Stansfield: initialize the distance matrix $\hat{\mathbf{D}}$ of the Stansfield estimator with $\hat{\boldsymbol{\theta}}_{\mathrm{LS}}$, and calculate $\hat{\boldsymbol{\theta}}_{\mathrm{SE}}$ with (15).

Note that these suboptimal algorithms can also be used in ML initialization.

The suboptimal algorithms alleviate computational burden, although they can introduce bias. The error mainly results from: 1) geometric distortion, and 2) approximating non-Gaussian with Gaussian noise. The former is straightforward. As for the latter, since a circular reflecting surface leads to nonlinear transformation, the measurement uncertainty of the target is no longer Gaussian. However, the suboptimal estimators employ sensor image based modeling, which implies that the target spatial uncertainty is Gaussian with regard to the sensor images, and that the uncertainty span linearly relates to the image-target distance $d_i(x_t,y_t)$. Actually, a circular surface may somewhat reduce this uncertainty expansion as shown in Fig. 7, and it is smaller than that of a flat surface due to *focusing*. This will be revealed via numerical simulation in Section 5.

Note that: 1) If the target is close to the reflecting surface and the ε_is are not very large, the situation that the uncertainty boundaries cross each other and sharply expand will not happen. 2) The ML in Section 3 assumes Gaussian distribution too. However, the nonlinear transformation (33) guarantees the shrink of target location uncertainty as shown in Fig. 7.

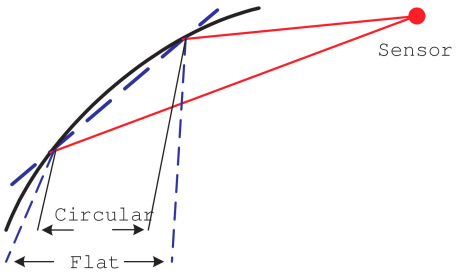

Fig. 7. Converting AoA uncertainty to target location uncertainty after flat (dashed) and circular (solid) reflections. The uncertainty span is linearly enlarged with the increase of $d_i(x_t, y_t)$ for the former, while the conical angle for the latter is somewhat reduced (focused, actually) after reflection.

TABLE II
Coordinates of Target and Sensors for Flat Reflecting Surfaces (m)

	Target	Sensor 1	Sensor 2	Sensor 3
x	10000	−3300	0	5000
y	5000	0	0	−2500

5. NUMERICAL RESULTS

5.1. Flat Reflecting Surfaces

This part compares the performance of LS, Stansfield, and ML estimators for flat reflecting surfaces. Three distributed sensors are employed in the simulation; their coordinates together with those of the target are in Table II. A LOS measurement is assumed unavailable, and three passive sensors extract AoAs of a target of interest with the help of their individual reflecting surfaces, of which the corresponding slope-intercept expressions are

$$\begin{aligned} &\text{Surface 1: } y = x/2 + 5000 \\ &\text{Surface 2: } y = -2500 \\ &\text{Surface 3: } y = x - 10000. \end{aligned} \tag{46}$$

Sensors are not perfect; measurement uncertainty (additive zero-mean Gaussian noise), exists. For simplicity of comparison, observation noises share the same variance: $\sigma_i^2 = \sigma^2$ for $\forall i$. The RMSEs versus standard variance σ for these three estimators together with CRLB are illustrated in Fig. 8. The number of Monte Carlo runs is 1000. According to Fig. 8, we observe

- The four curves linearly depend on σ;
- LS is biased and is the worst among them, while the RMSE of Stansfield is close to that of ML.

Simulation results coincide with the theoretical analysis for LOS bearings-only localization in [6], [10], [13], [19]. This is not surprising because NLOS bearing-only localization is mathematically equivalent to that of LOS.

The estimate of the Stansfield rather than the LS estimator is used to initialize the ML, as the former has slightly better localization accuracy than the latter for flat reflecting surfaces. Then, gradient-based approach

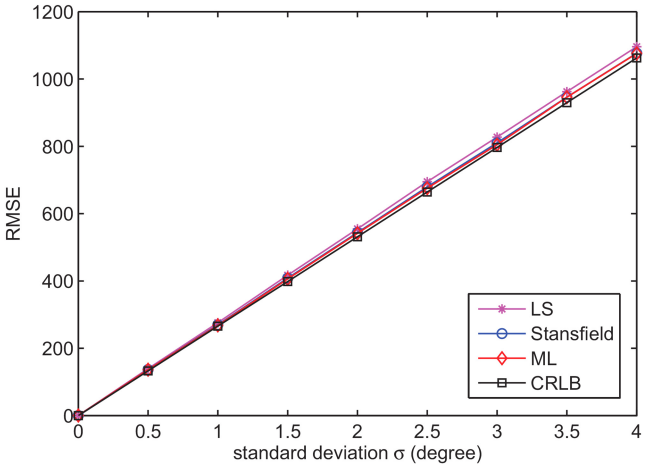

Fig. 8. Example of RMSEs versus bearing standard deviation σ for flat reflecting surfaces.

TABLE III
Polar Coordinates of the Target and Sensors for the Circular Reflecting Surface: Parameter set A

	Target	Sensor 1	Sensor 2	Sensor 3	Sensor 4
r_d (km)	$r + 50$	r	r	r	r
ϕ (π)	0	0.10	0.08	−0.09	−0.06

TABLE IV
Polar Coordinates of the Target and Sensors for the Circular Reflecting Surface: Parameter set B

	Target	Sensor 1	Sensor 2	Sensor 3
r_d (km)	$r + 50$	r	r	r
ϕ (π)	0	0.11	−0.07	−0.12

is employed to search for the optimal solution of ML based on (6). The computational complexity of each method here is similar to the corresponding one for the LOS based location [6, 10, 13, 19].

5.2. Circular Reflecting Surface

Bearings-only localization with a circular reflecting surface is investigated in this subsection. Here the reflecting and blocking circles are concentric, with center $(0,0)$; their radii are, respectively, $R = 6671$ km and $r = 6371$ km. Two system parameter sets are used, and the coordinates of the target and sensors are collected in Tables III and IV, respectively. The coordinates are polar for simplicity, and they can be easily converted into Cartesian via $(r_d\cos(\phi), r_d\sin(\phi))$. All sensors share the same noise variance $\varepsilon_i^2 = \varepsilon^2$ as the previous case. Example of RMSEs versus ε for LS, Stansfield, and ML estimators for those two configurations are shown in Fig. 9, where the number of runs is 1000.

From those two figures, we observe:

- RMSEs for Stansfield and LS may still linearly depend on ε; however, the former is not necessarily

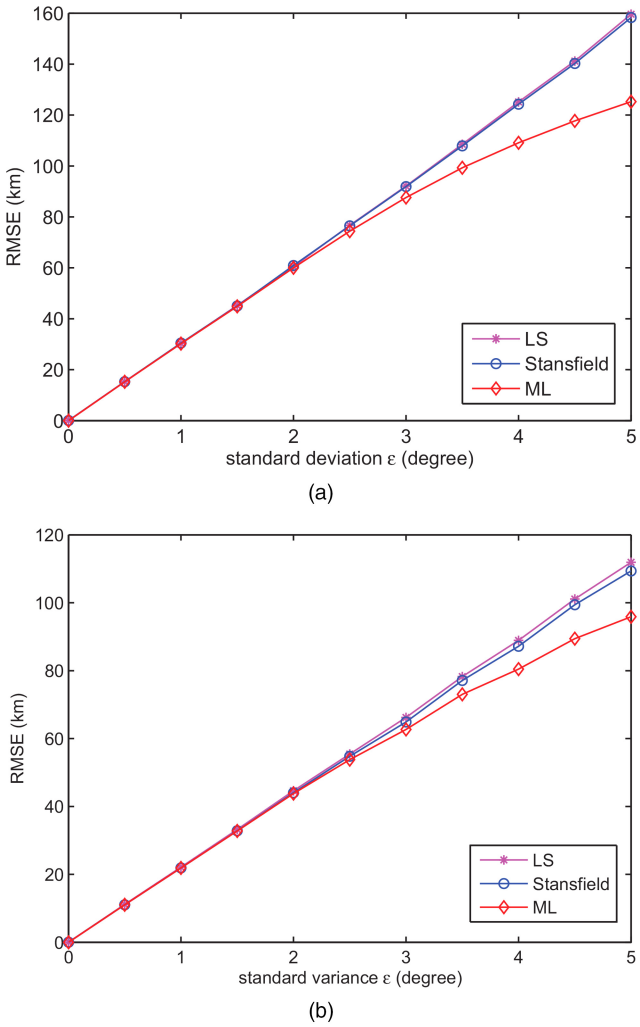

Fig. 9. Example of RMSEs versus AoA standard variance ε for a circular reflecting surface with circular block.

better than the latter. This may result from the fact that multiple approximations, such as arc, noise, and small-angle, are employed in the Stansfield estimator for the circular surface, and these may degrade its accuracy.

- ML outperforms LS and Stansfield at high ε; however, the difference is not significant for small noise levels. This is expected in that for a small variance the uncertainty area is small, and the suboptimal approximations are nearly exact.
- The RMSE for ML is not a linear function of ε, since reflection with a circular surface may shrink the uncertainty area compared to the flat one.

Apparently the Stansfield method does not significantly outperform LS in this case, so a system designer can make a choice between LS and ML trading off computation for estimation accuracy. In addition, various simulations reveal that $\varepsilon = 1.5$ would be small enough for the fearless use of suboptimal estimators in target localization.

The estimate of LS is used to initialize the ML in this part. Specifically, we firstly set the LS estimate as the center of a 160×200 km^2 rectangle, and then uniformly divide it into 1×1 km^2 grids. The ML estimate is the point with the maximal likelihood value among these 161×201 vertices. The computational complexity of the LS and Stansfield estimators are similar to those for the LOS case [6, 10, 13, 19]. However, that for the ML is much higher than its counterpart due to the grid search and solution elimination.

The received signal of an OTHR usually undergoes long distance propagation as well as frequency dependent reflection loss. Those can result in a low signal-to-noise ratio (SNR), which will cause low angular accuracy. For example, reference [17] points out that a tapered aperture of 3 km will lead to an angular resolution as large as 4 deg if the OTHR is operated at 3 MHz. Thus, a standard deviation up to 5 deg would be reasonable in simulation, even though it sounds large for traditional LOS radar systems such as phased array.

6. CONCLUSION

This paper studies bearings-only target localization with NLOS reflection measurements. Two kinds of reflecting surfaces are investigated: flat and circular. We derive the LS, Stansfield, and ML algorithms for both of them, and their performances are analyzed both via theory and algorithmically.

The reflecting surfaces are idealized and assumed known; however, the practical situation has many ingredients not discussed in this paper. For example, sensors need not be synchronized, in which case a dynamic component (tracking, or at least motion vector estimation) must be added. Multiple targets may also be present, in which case some means of data association is required. A practical system must also allow for nonidealities, such as of errors in sensor position and reflection surface, with possible extension of the circular results to the elliptical case.

Lastly, and probably most important, a real OTHR system operates in three dimensions. The estimators derived in this manuscript can easily be extended from the circular to the spherical case. But although we fully expect the existence and uniqueness statements (Lemmas 1, 2, and 3) to be extensible (and very interestingly so) to three dimensions, we doubt that this would be straightforward.

APPENDIX

6.1. Image of Specular Reflection with Flat Surface

LEMMA 4 *The image of a point (x_0, y_0) with respect to a flat reflecting surface $y = ax + b$ locates at $(\bar{x}_0, \bar{y}_0)$ in two dimensions, where*

$$\begin{aligned} \bar{x}_0 &= \frac{1-a^2}{1+a^2}x_0 + \frac{2a}{1+a^2}y_0 - \frac{2ab}{1+a^2} \\ \bar{y}_0 &= \frac{2a}{1+a^2}x_0 + \frac{a^2-1}{1+a^2}y_0 + \frac{2b}{1+a^2}. \end{aligned} \tag{47}$$

PROOF Proof is straightforward.

Lemma 4 is not universal: if the surface overlaps with $x = c$ (the special case is not included in $y = ax + b$), the image location is $(\bar{x}_0 = 2c - x_0, \bar{y}_0 = y_0)$. However, this special case can be easily avoided via a proper coordinate rotation, so we will no longer separately discuss it in target localization.

6.2. Equivalence: Target and Sensor Images Based Modelings

The equivalence of the target and sensor images based modelings without noise are proven via $\tan\phi_i = \tan\phi_i'$ in the following:

$$\begin{aligned}\tan\phi_i &= \frac{\tan(2\arctan a_i) - \dfrac{y_t - \bar{y}_i^s}{x_t - \bar{x}_i^s}}{1 + \tan(2\arctan a_i)\dfrac{y_t - \bar{y}_i^s}{x_t - \bar{x}_i^s}} \\ &= \frac{\dfrac{2a_i}{1 - a_i^2} - \dfrac{y_t - \bar{y}_i^s}{x_t - \bar{x}_i^s}}{1 + \dfrac{2a_i}{1 - a_i^2} \cdot \dfrac{y_t - \bar{y}_i^s}{x_t - \bar{x}_i^s}} \\ &= \frac{2a_i(x_t - \bar{x}_i^s) - (1 - a_i^2)(y_t - \bar{y}_i^s)}{(1 - a_i^2)(x_t - \bar{x}_i^s) + 2a_i(y_t - \bar{y}_i^s)} \end{aligned} \tag{48}$$

Substitute (4) into (48), we have

$$\begin{aligned}\tan\phi_i &= \frac{2a_i x_t + (a_i^2 - 1)y_t + 2b_i - (1 + a_i^2)y_i^s}{(1 - a_i^2)x_t + 2a_i y_t - 2a_i b_i - (1 + a_i^2)x_i^s} \\ &= \frac{\bar{y}_i' - y_i^s}{\bar{x}_i' - x_i^s} = \tan\phi_i'. \end{aligned} \tag{49}$$

REFERENCES

[1] C. R. Berger, S. Choi, S. Zhou, and P. Willett
Channel energy based estimation of target trajectories using distributed sensors with low communication rate.
IEEE Transactions on Signal Processing, **58**, 4 (Apr. 2010), 2339–2350.

[2] W. D. Blair and M. Brandt-Pearce
Statistics of monopulse measurements of Rayleigh targets in the presence of specular and diffuse multipath.
In *Proceedings of the IEEE Radar Conference*, Atlanta, GA, May 2001.

[3] S. Boyd and L. Vandenberghe
Convex Optimization.
Cambridge University Press, Cambridge, U.K., 2004.

[4] L. Chen, Q. Li, W. Guo, and Y. Zhu
One-dimensional mirrored interferometric aperture synthesis.
IEEE Geoscience and Remote Sensing Letters, **7**, 2 (Apr. 2010), 357–361.

[5] J. W. Ciboci
Over-the-horizon radar surveillance of airfields for counterdrug applications.
IEEE Aerospace and Electronic Systems Magazine, **13**, 1 (Jan. 1998), 31–34.

[6] K. Doğançay
On the bias of linear least squares algorithms for passive target localization.
Signal Processing, **84**, 3 (Mar. 2004), 475–486.

[7] K. Doğançay
Bearings-only target localization using total least squares.
Signal Processing, **85**, 9 (Sept. 2005), 1695–1710.

[8] M. Drexler and M. J. Gander
Circular billiard.
SIAM Review, **40**, 2 (1998), 315–323.

[9] R. L. Fante and S. Dhar
A model for target detection with over-the-horizon radar.
IEEE Transactions on Aerospace and Electronic Systems, **26**, 1 (Jan. 1990), 68–83.

[10] M. Gavish and A. J. Weiss
Performance analysis of bearing-only target location algorithms.
IEEE Transactions on Aerospace and Electronic Systems, **28**, 3 (Aug. 1992), 817–828.

[11] K. C. Ho, X. Lu, and L. Kovavisaruch
Source localization using TDOA and FDOA measurements in the presence of receiver location errors: Analysis and solution.
IEEE Transactions on Signal Processing, **55**, 2 (Feb. 2007), 684–696.

[12] J. E. Howard
Time-dependent circular billiard.
Mathematical Problems in Engineering, 1 (2009), 1–10.

[13] L. M. Kaplan, Q. Le, and P. Molnar
Maximum likelihood methods for bearings-only target localization.
In *Proceedings of the International Conference on Acoustics, Speech and Signal Processing*, Salt Lake City, UT, May 2001.

[14] L. F. McNamara
The Ionosphere: Communications, Surveillance, and Direction Finding.
Malabar, FL: Kreiger, 1991.

[15] N. Mukhopadhyay
Probability and Statistical Inference.
Marcel Dekker Inc., New York, 1st ed., 2000.

[16] P. M. Neumann
Reflections on reflection in a spherical mirror.
American Mathematical Monthly, **105**, 6 (1998), 523–528.

[17] R. J. Riddolls
A Canadian perspective on high frequency over-the-horizon radar.
Defence R&D Canada, Ottawa, http://cradpdf.drdc.gc.ca/PDFS/unc64/p527279.pdf.

[18] X. Song, P. Willett, and S. Zhou
Target localization with NLOS circularly reflected AoAs.
In *Proceedings of the International Conference on Acoustics, Speech and Signal Processing*, Prague, Czech, May 2011.

[19] R. G. Stansfield
Statistical theory of DF fixing.
Journal of the IEE, **14**, 15 (Dec. 1947), 762–770.

[20] P. Stoica and A. B. Gershman
Maximum-likelihood DOA estimation by data-supported grid search.
IEEE Signal Processing Letters, **6**, 10 (Oct. 1999), 273–275.

[21] I. Ziskind and M. Wax
Maximum likelihood localization of multiple sources by alternating projection.
IEEE Transactions on Signal Processing, **36**, 10 (Oct. 1988), 1553–1560.

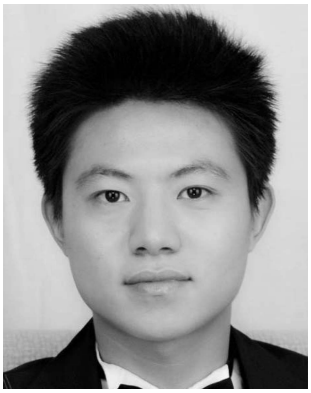

Xiufeng Song (S'08) received the B.S. degree from Xidian University, Xi'an, China, in 2005, the M.S. degree from Institute of Electronics, Chinese Academy of Sciences (CAS), Beijing, China, in 2008, and the Ph.D. degree from University of Connecticut, in 2012, all in electrical engineering.

Dr. Song is currently working at the LSI Corporation, San Jose, CA. His research interests lie in signal processing, detection, estimation, and tracking. He received the Best Student Paper Award (second place) at the 2012 IEEE Sensor Array and Multichannel Signal Processing Workshop.

Peter Willett (F'03) received his B.A.Sc. (engineering science) from the University of Toronto in 1982, and his Ph.D. degree from Princeton University in 1986.

Dr. Willett has been a faculty member at the University of Connecticut ever since, and since 1998 has been a professor. His primary areas of research have been statistical signal processing, detection, machine learning, data fusion and tracking. He has interests in and has published in the areas of change/abnormality detection, optical pattern recognition, communications and industrial/security condition monitoring.

He was editor-in-chief for *IEEE Transactions on Aerospace and Electronic Systems* from 2006–2011, and is presently the VP of Publications for the IEEE AESS. In the past he has been associate editor for three active journals—*IEEE Transactions on Aerospace and Electronic Systems* (for Data Fusion and Target Tracking) and *IEEE Transactions on Systems, Man, and Cybernetics, parts A and B*. He is also associate editor for the *IEEE AES Magazine*, associate editor for ISIF's electronic *Journal of Advances in Information Fusion*. He was General Co-Chair (with Stefano Coraluppi) for the 2006 ISIF/IEEE Fusion Conference in Florence, Italy, Executive Chair of the 2008 Fusion Conference in Cologne, and Emeritus Chair for the 2011 Fusion Conference in Chicago. He was Program Cochair (with Eugene Santos) for the 2003 IEEE Conference on Systems, Man & Cybernetics in Washington, D.C., and Program Cochair (with Pramod Varshney) for the 1999 Fusion Conference in Sunnyvale. He has been a Member of the IEEE Signal Processing Society's Sensor-Array & Multichannel (SAM) Technical Committee since 1997, and both serves on that TC's SAM Conferences' Program Committees and maintains the SAM website.

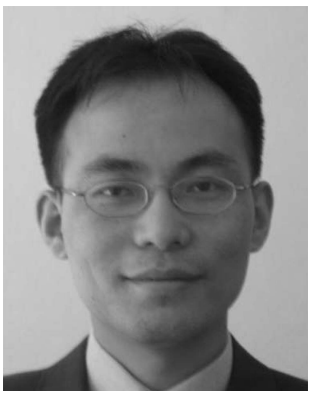

Shengli Zhou (SM'11) received the B.S. degree in 1995 and the M.Sc. degree in 1998, from the University of Science and Technology of China (USTC), Hefei, both in electrical engineering and information science. He received his Ph.D. degree in electrical engineering from the University of Minnesota (UMN), Minneapolis, in 2002.

He has been an assistant professor with the Department of Electrical and Computer Engineering at the University of Connecticut (UCONN), Storrs, 2003–2009, and now is an associate professor. He holds a United Technologies Corporation (UTC) Professorship in Engineering Innovation, 2008–2011. His general research interests lie in the areas of wireless communications and signal processing. His recent focus is on underwater acoustic communications and networking.

Dr. Zhou served as an associate editor for *IEEE Transactions on Wireless Communications*, Feb. 2005–Jan. 2007, and *IEEE Transactions on Signal Processing*, October 2008–October 2010. He is now an associate editor for *IEEE Journal of Oceanic Engineering*. He received the 2007 ONR Young Investigator award and the 2007 Presidential Early Career Award for Scientists and Engineers (PECASE).